Lagrangian stochastic modelling of liquid flow in a mechanically agitated vessel

Sheikh, Hamzah; Savari, Chiya; Barigou, Mostafa

DOI:
10.1016/j.ces.2021.117318

Document Version
Peer reviewed version

Citation for published version (Harvard):
Sheikh, H, Savari, C & Barigou, M 2022, 'Lagrangian stochastic modelling of liquid flow in a mechanically agitated vessel', *Chemical Engineering Science*, vol. 249, 117318. https://doi.org/10.1016/j.ces.2021.117318

Lagrangian Stochastic Modelling of Liquid Flow in a Mechanically Agitated Vessel

Hamzah A. Sheikh, Chiya Savari, Mostafa Barigou

School of Chemical Engineering, University of Birmingham, Edgbaston, Birmingham, B15 2TT, UK

Abstract

Deterministic models of complex flows are challenging and computationally expensive. We propose here, for the first time, a computationally efficient data-driven Lagrangian stochastic approach to predict liquid flow inside a mechanically agitated vessel. The model relies on the input of a short driver data set to predict the full flow field. We investigate the capability of zeroth, first and second order models over a wide range of flow conditions including different impeller configurations and rotational speeds. The first and second order models provide good predictions of local flow properties, with the first order model being slightly superior. The technique is also capable of predicting flow well outside the range of experimental conditions.

Keywords: fluid flow, Lagrangian trajectory, mixing, PEPT, stirred vessel, stochastic model.

1. Introduction

Numerous process industries depend on the mixing of liquids and particle-liquid mixtures including the manufacture of pharmaceuticals, foods, cosmetics, plastics, minerals, nuclear and petroleum industries. Mixing operations are often conducted in mechanically agitated vessels and understanding of the complex flow dynamics in these processing units is vital for the effective design of products and processes. Various theoretical approaches exist for modelling of mixing flows, including different computational fluid dynamics (CFD) techniques. With the advancement of computing capability, models for describing turbulence are getting increasingly more reliable. In particular, with the aid of high-powered computing, turbulence can be determined using direct numerical simulation (DNS). By using a mesh with elements smaller than the Kolmogorov length scale, DNS solves the Navier-Stokes equations directly without a turbulence model down to the Kolmogorov time scale. This deterministic approach is extremely computationally expensive and is not practical for most engineering applications. As a result, the majority of Eulerian numerical deterministic approaches such as Reynolds averaged Navier-Stokes (RANS) or large eddy simulation (LES) utilise a turbulence model, and include time-averaging or space-filtering (Joshi & Nayak 2019).

Alternatively, turbulence can be handled by using a Lagrangian stochastic model (LSM) in combination with Eulerian methods. In a LSM, the positions are advanced in space over a given time step and are subject to random perturbations, defined by the Wiener process (Gardiner, 2004). These hybrid methods often give good results whilst reducing computational expense. For example, using a RANS simulation where turbulence velocities were calculated using a LSM, Marshall & Sala (2011) obtained accurate predictions of the growth of algae in photobioreactor flows at a fraction of the computational cost of a DNS simulation. By contrast, a fully Lagrangian method can be used without relying on Eulerian data generated from a RANS or LES simulation. Israelsson et al. (2006) compared three techniques of Lagrangian modelling for environmental applications; forward Gaussian puff tracking (FGPT), backward Gaussian puff tracking (BGPT), and LSM (referred to as random walk particle tracking, RWPT). They showed that out of the three methods, the LSM was applicable to complex velocity or diffusivity fields and produced more accurate results than Eulerian methods, even though it was not the most computationally efficient.

Dehling et al. (2007) used a fully-Lagrangian computational approach to model slug rise in a fluidised bed. Generally, the study showed good agreement with experimental data, especially

with a single type of particle. When a second type of particle was introduced, there was more deviation. However, the authors suggested the system would be difficult if not impossible to model using a deterministic approach. The method was later improved by Farzaneh et al. (2011) who used a multigrid approach to model fuel mixing in fluidised beds. The fuel and inert particles having a distinct size and density difference would be difficult to model using Dehling et al.'s approach. The multigrid approach yielded good agreement of average trajectories of fuel particles with experimental data under a variety of conditions. Recently, Rezavand et al. (2019) reported a fully-Lagrangian computational model for the integration of mixing and biochemical reactions in anaerobic digestion. The 2D domain was discretised into particles, each containing the information of biologically active compounds. The continuity and momentum equations were discretised using smooth particle hydrodynamics (SPH) along with the Fickian advection-diffusion equation. The result was a discretised Lagrangian set of equations not involving the Eulerian framework, affording the benefit of direct observation of the impact of mixing on biogas production, information that would otherwise be lost through an Eulerian scheme. Predictions were in good agreement with experimental data.

The RWPT model was also adopted by Nordam et al. (2019) who compared the application of a LSM against Eulerian methods to the vertical transport of buoyant material in a water column. The LSM was capable of capturing the discrete Lagrangian flow behaviour of oil droplets, fish eggs, and microplastics by using a large ensemble of particles to describe the effects of advection and diffusion. Particles were progressed in time with a random perturbation, using a random walk algorithm known as the Visser scheme. Excellent agreement was obtained between the stochastic and deterministic models, due to the importance given to the boundary conditions in the Lagrangian scheme.

An alternative hybrid method also exists, whereby a Eulerian field is already available to impose Lagrangian particles into. This method is often used in environmental studies; see for example Gleicher et al. (2014) and Ferrero & Oettl (2019). The former study used a LSM to model the dispersion of pathogenic spore particles that cause disease in plant canopies, whilst the latter built on the LSM by implementing the Langevin equations proposed by Thomson (1987) to include the effects of concentration-variance dissipation. Results in both cases demonstrated the LSM's high potential to predict the movement of particles in a known velocity field, without the computational cost of a deterministic approach. This approach has also been exploited in engineering applications. Matos et al. (2018) illustrated the ability of a

LSM to track particles to describe the front of a fluid in a confined impinging jet reactor, with the aid of a transient Eulerian velocity field from a CFD simulation. The model allowed for the calculation of interfacial area generation, which was found to grow at an exponential rate in chaotic flows and at a linear rate in steady flows. Therefore, it appears that the LSM strategy in a known velocity field is likely to be suitable for dealing with mixing problems, with the added benefit of low computational cost.

The data-driven LSM technique has not been used to model mixing systems. In this study, we propose a simple yet accurate approach to model turbulent single-phase flow in a mechanically agitated mixing vessel. The Eulerian velocity fields are experimentally determined using a positron emission particle tracking (PEPT) technique. By applying a LSM to these experimental flow fields, a simplified data-driven model is developed to predict flow behaviour.

2. Experimental

2.2 Mixing vessel apparatus

The flow and mixing of single-phase water was studied in a mixing vessel of diameter T = 288 mm and a liquid height $H = T$, as illustrated in Fig. 1a. Agitation was achieved using a 6-blade 45^o pitched-blade turbine (PBT) or a 6-blade Rushton disc turbine (RDT) of diameter $D = T/2$, impeller blade width $W = T/10$, baffle width $B = T/10$ and impeller clearance $C_{imp} = T/4$ for PBT and $T/3$ for RDT. The pitched blade turbine was operated in either up-pumping (PBTU) or down-pumping mode (PBTD). A radioactively-labelled resin tracer particle was used to track the flow. The resin particle was made neutrally-buoyant by adding salt to the water to match its density. Experiments were run at different impeller rotational speeds (100-500 rpm) to determine in each case the long-term trajectory of the liquid.

2.2 Positron emission particle tracking

PEPT is a non-intrusive method by which a positron emitting tracer particle is accurately tracked within process equipment, providing three-dimensional space and time data for a long-term Lagrangian trajectory (Barigou 2004, Sadrmomtaz et al., 2007). PEPT is able to image flow in opaque fluids and opaque equipment, unlike optical methods such as particle image velocimetry (PIV) and laser Doppler velocimetry (LDV), but with comparable accuracy (Pianko-Oprych et al., 2009). In PEPT each component in a multiphase flow can be tracked individually to determine its 3D Lagrangian trajectory. PEPT has been extensively used to

study flow and mixing in stirred vessels. More details of the technique can be found in our earlier papers (Guida et al., 2010a, 2010b & 2011).

3. Lagrangian stochastic modelling

Stochastic models are used to predict various outcomes of a given system by applying random perturbations to pre-determined variables. As few processes are deterministic, stochastic models can be utilised to give the probability of a certain result. This use of probability can be exploited, for example, to model the Brownian motion of particles or fluid parcels and has previously been used to predict propagation of atmospheric pollutants (Bergin & Milford, 2000), diffusion in oceanography (Ruplo, 2006) and dissipation of odours (Ferrero & Oettl, 2019). Deterministic models for complex flow system are challenging and computationally demanding. Instead, stochastic models adopt a simplified structure, greatly reducing computational cost whilst having the ability to predict complex flow characteristics. In consequence, this approach seems to have potential for modelling fluid flows, in particular inside stirred mixing vessels. In a LSM, fluid parcel positions are advanced in space over a given time step via random perturbations. The basic structure of a LSM algorithm is depicted in Fig. 2 and discussed in detail in the section below. Simulation time is similar to the run time of an actual experiment, for example, to compute a one hour trajectory the computational time is around one hour for a first order model.

3.1. Input velocity field

The Lagrangian stochastic model is data driven, i.e., experimental 3D mean velocities from the system form the basis of the operation of the model (Fig. 2). An initial particle position is set and is advanced in space over a given time step. Depending on the order of the model, different flow parameters are subjected to random perturbations defined by the Wiener process and described by a Gaussian distribution with unit variance (Gardiner 2004). For the model to yield suitable results, an appropriate experimental velocity field must be used. Here, Lagrangian PEPT velocity data acquired in a stirred vessel were converted to a Eulerian velocity field. By dividing the vessel volume into a grid of equal volume cells, as shown in Fig. 1b, the local time-averaged velocity of each flow component was obtained inside each cell (Fig. 1c).

Grid mesh density requires careful selection, given the way LSM re-calculates the position of the particle when it leaves (i.e., collides with) the system boundary. Thus, optimising the cell size near the wall of the vessel is vital for simulations. Too coarse a mesh leads to the cell

nearest the wall being too large. The average velocity in such a cell is often directed towards the boundary away from the centre of the tank. If LSM calculates the particle to be in this cell, it is likely to collide with the vessel wall and require re-calculation of position. If a collision model is used, the particle is again likely to enter the same cell due to its size, resulting in a repeating process of the particle colliding with the vessel wall. The opposite case can also pose an issue, as the trajectory data from a PEPT experiment have a finite number of positions and in many cases will not occupy all cells in a mesh if their size is very small. This results in a 'zero' cell; a cell which has no velocity associated with it. If the particle enters a cell with no velocity associated with it, it will remain stationary in the cell for the duration of the simulation, as shown further below (Equations 1-9). Mesh size is dependent on the time step selected for the model and in an ideal scenario, the particle should move into an adjacent cell to prevent any repeating movement especially at the boundary. As the mean temporal resolution of the experimental PEPT data is 5 ms, this value was assigned as the time step for the model and a mesh density study was conducted on sample experimental trajectories to establish a suitable grid for the model.

In general, the aim of LSM is to be able to use a short experimental particle trajectory to predict the long-term trajectory of the particle under similar conditions. In this case, the particle in question is the PEPT tracer particle used to track the liquid motion inside the stirred vessel. A trajectory length of 5 min was selected as an input to the model as it was sufficient for a particle tracer to visit the majority of the computational grid cells and find a representative velocity field. Fig. 3 illustrates the number of detected positions in each mesh cell under different experimental conditions. Mesh size was adjusted in the r and z-directions with a set number of cells in the θ-direction. Once appropriate cell dimensions were determined for the r and z-directions, the number of cells in the θ-direction was adjusted and assessed in the same way.

Determining the ideal mesh density is a compromise. Increasing the number of cells improves the fidelity of the velocity field but increases the risk of cells with no detection points and, hence, missing local velocity values. A cell with no detections cannot be used in the model as it results in stalling of the model particle and causes the model to fail. Reducing the number of cells, on the other hand, can also be detrimental as it may reduce resolution to the point where the local velocity field is no longer a true representation of the actual flow. Fig. 3 shows the effect of varying the grid mesh density on the number of detected positions in each cell. All cells contain detected positions when $N_r = 5$ and $N_z = 10$. Fewer detections tend to be found

near the top of the vessel because liquid agitation is less intense in this region. Increasing the number of cells in both directions results in fewer detected positions per cell, with increasingly more 'zero' cells appearing near the top and the centre of the vessel (N_r = 20, N_z = 40). These numerical tests led to an optimised grid of 2400 equal volume cells where N_θ = 12, N_r = 10 and N_z = 20, which yielded the highest resolution for the velocity field with the fewest cells containing zero detections. To prevent the failure of the model, as pointed out above, where a 'zero' cell is found, the cell is assigned an estimated velocity value using a linear 3D grid interpolation.

3.2. Model equations

There are three orders of stochastic model to describe the motion of a particle over time: zeroth, first and second order (Fig. 2). The form of these models used in this study, was adopted from the oceanography works of Ruplo (2006) and LaCasce (2008). Along with velocity field information, LSM requires knowledge of decorrelation times when utilising a first or second order model. Velocity and acceleration time signals obtained from the experimental PEPT trajectory were used to estimate these decorrelation times (Guida et al., 2010b). Decorrelation times for velocity and acceleration were calculated in each direction over 1 min intervals along a 5 min trajectory, as summarised in Table 1, and an average value taken. LSM uses this information to scale the amount of stochastic noise added to the system, with an inverse relationship. If decorrelation times are short, i.e. the system decorrelates and loses its memory quickly which reflects a high degree of stochasticity, thus the stochastic noise added is large. By contrast, if the time taken to decorrelate is large, the level of turbulence is less and therefore less stochastic noise is added.

The zeroth order model is the simplest variation of LSM, where particle position is progressed using the following set of equations (Ruplo, 2006; LaCasse, 2008):

$$x_i^{t+dt} = x_i^t + dx_i^{dt} \tag{1}$$

$$dx_i^{dt} = \bar{U}_\iota dt + \sqrt{2\bar{U}_\iota^{\,2}}\,(dw^{dt})^2 \tag{2}$$

where, x_i and $\bar{U}_\iota$ are, respectively, the particle position and mean particle velocity in the *i*-direction, and dw^{dt} is the Wiener process for the time step *dt*, which is discretised as follows:

$$dw^{dt} \approx \sqrt{dt}\, N(0,1) \tag{3}$$

where, $N(0,1)$ is a normal distribution with a mean of 0 and unit variance.

In the first order model, Eq. (2) above is replaced by the following equations:

$$dx_i^{dt} = \left(u_i^{t+dt} + \bar{U}_\iota\right)dt \tag{4}$$

$$u_i^{t+dt} = u_i^t + du_i^{dt} \tag{5}$$

$$du_i^{dt} = -\frac{u_i^t}{T_{u,i}}dt + \sqrt{\frac{2\bar{U}_\iota^{\,2}}{T_{u,i}}}\, dw^{dt} \tag{6}$$

where, u_i and $T_{u,i}$ are, respectively, the local velocity and the velocity decorrelation time in the *i*-direction.

In the second order model, Eq. (6) above is replaced by the following equations:

$$du_i^{dt} = a_i^{t+dt} - \frac{u_i^t}{T_{u,i}} \tag{7}$$

$$a_i^{t+dt} = a_i^t + da_i^{dt} \tag{8}$$

$$da_i^{dt} = -\frac{a_i^t}{T_{a,i}}dt + \sqrt{2\bar{U}_\iota^{\,2}\frac{T_{a,i}+T_{u,i}}{T_{a,i}T_{u,i}}}\,(dw^{dt})^{-1} \tag{9}$$

where, a_i and $T_{a,i}$ are, respectively, the local acceleration and the acceleration decorrelation time in the *i*-direction.

3.3. Boundary collision

Due to the nature of LSM, the simulated tracked particle is able to leave the solid boundary of the flow field if not restricted. A check is conducted after each new particle position is computed, as illustrated in the algorithm flowchart (Fig. 2). If the particle is outside of the flow domain (in this case the stirred vessel), then there are two possible methods for re-inserting it into the flow:

(i) Random particle injection (RPI): the particle position outside the boundary is discarded and replaced with a random position within the boundary, and the LSM is re-initiated.

(ii) Collision model (CM): the previous position and current position are used to calculate the particle's momentum and, thus, a new particle position inside the flow domain is computed assuming an elastic collision with the vessel wall.

In this case, given the high frequency of boundary collisions with the vessel wall, the RPI method resulted in numerous kinks in the particle trajectory leading to erroneous results. In contrast, the CM method yielded a much more realistic trajectory. Thus, experimental PEPT particle-wall interactions were analysed and results were implemented into the collision model.

Lagrangian data obtained from PEPT experiments are in the form of discrete space-time positions of a tracer particle. Some collisions can be easily identified as a clear interaction with the vessel wall is observed. There are, however, collisions which are hidden in the data as they occur between the recordings of space-time data of the tracer but these cannot be included in collision modelling because of the missing information.

Particle-wall collisions can be compared by analysing the ratio between tracer velocity before and after the collision, using an arbitrary collision factor C_f which can be defined in either of two ways, as follows:

$$C_f = \frac{v_2}{v_1} \tag{10}$$

where, v_1 is the total velocity of the particle prior to collision with the vessel wall, and v_2 is the total velocity of the particle after collision with the vessel wall; or alternatively taking into consideration the angle of collision with the vessel wall ϕ:

$$C_f = \frac{1}{\tan(\phi)} \tag{11}$$

where, ϕ is defined as:

$$\tan(\phi) = \frac{\|\mathbf{v_i} \times \mathbf{v_r}\|}{\mathbf{v_i} \cdot \mathbf{v_r}} \quad (12)$$

where, $\mathbf{v_i}$ and $\mathbf{v_r}$ are the particle incident and rebound velocity vectors, respectively. A C_f value < 1 indicates a collision angle larger than 45°, and C_f > 1 indicates a collision angle smaller than 45°.

Typical experimental data are plotted in Fig. 4, showing a distribution of C_f values for both definitions of C_f. The mean C_f value in Fig. 4(a) is close to 1, indicating perfectly elastic collisions irrespective of the ratio of local values of the shear and normal velocities and the particle-wall contact angles. The data in Fig. 4(b) shows a mean C_f value close to 0, i.e. $\phi \approx 90^o$, indicating again almost perfectly elastic collisions. It should be noted that the value of C_f is affected not only by the nature of the collision, but also by the oncoming flow which may impart additional momentum to the bouncing particle. A sensitivity analysis of LSM-predicted time-averaged velocity profiles in cells adjacent to the vessel wall to the value of C_f adopted is presented in Fig. 5. Despite the wide range of C_f values tested, the LSM-predicted velocity field close to the vessel wall was not sensitive to the definition of C_f or the value adopted. Based on this sensitivity analysis, it was clear that either definition C_f could be used with no significant effects on the predicted velocity profiles. Therefore, Eq. (10) was adopted in all the calculations as it was less computationally demanding, with an arbitrary value $C_f = 1$.

4. Results and discussion

LSM was used to calculate three-dimensional Lagrangian fluid trajectories in a mixing vessel. The zeroth order model (Eqs. 1-2) failed to produce sufficiently accurate predictions, thus, detailed analyses are presented here only for the first and second order models, denoted, respectively, by ^{1}LSM and ^{2}LSM. The computations were executed in MATLAB with a time step dt = 5 ms, of the same order as the data acquisition time step achieved in PEPT. The time to compute a 40 min long trajectory via ^{1}LSM was ~ 30 min, whilst ^{2}LSM took nearly twice as long. Such a computational cost is very small in comparison with all known deterministic models.

In order to evaluate the performance of the approach, detailed quantitative comparisons of LSM predictions and PEPT experiments were conducted throughout the stirred vessel. The azimuthally averaged distributions of local velocity were compared at six different axial and

radial planes. Axial (vertical) planes were examined from the tip of the impeller ($r = 0.5R$) to the vicinity of the vessel wall ($r = 0.87R$). Radial (horizontal) planes were examined from the bottom of the vessel ($z = 0.03H$) to the top of the vessel ($z = 0.97H$), including a plane just below the impeller ($z = 0.17H$) and a plane just above the impeller ($z = 0.38H$).

4.1. Predicting long-term trajectories from short-term LSM driver trajectories

The potential benefit of using a stochastic model is the ability to use small sets of Lagrangian trajectory data pertaining to specific flow conditions to predict long-term trajectories. Here, we investigate the effects of the size of the initial data set used to drive the LSM on the accuracy of the predictions. The plots in Fig. 6 show the velocity profiles for 300 rpm PBTD predicted on the basis of short-term PEPT trajectories within the range 1 – 10 min. Results show that even a 1 min driver trajectory is generally adequate despite significant errors in some regions of the flow. Using a 3 min driver trajectory, the agreement between prediction and experiment is good throughout the flow domain. Beyond 3 min, there is no significant improvement in prediction accuracy. This minimum driver trajectory length depends slightly on the flow conditions, in particular the speed of the impeller. It tends to increase at lower impeller speeds as less data points are acquired per unit time, and reduce at higher speeds as the data acquisition rate is higher. Tests conducted at 100 rpm showed that 3 min was still satisfactory, but at 500 rpm this could be reduced down to 2 min. Erring on the safe side, we used 5 min driver trajectories throughout the rest of this study.

4.2. Model validation

To validate the ^{1}LSM and ^{2}LSM models, extensive PEPT experiments were conducted using the PBTD impeller running at speeds within the range 100 - 500 rpm. Experimental PEPT trajectories of 5 min length were used to drive the models (Fig. 2). The LSMs were used to produce 40 min long trajectories which were then compared to equivalent PEPT trajectories.

4.2.1. Velocity profiles

Azimuthally averaged profiles of local velocity components (v_r, v_z, v_θ) predicted by ^{1}LSM and ^{2}LSM are compared to PEPT data in Figs. 7-9 for the sample case of PBTD running at 300 rpm. Overall, both models were capable of predicting the velocity components well in all regions of the vessel across the whole range of impeller speeds used. Compared to PEPT, as observed in the vertical velocity profiles, ^{2}LSM tends to underpredict v_θ and v_z somewhat along

the horizontal impeller plane (Fig. 7, Fig. 8). Such underpredictions are also reflected in the horizontal velocity profiles close to the impeller plane (e.g., z = 0.17H, 0.38H), but they are overall less significant in the case of v_r (Fig. 9). In contrast, the [1]LSM model does not suffer from these errors. It should be noted, however, that these regions contain intense turbulence and high liquid velocities and the experimental measurements themselves are subject to some uncertainty, as shown in our previous work (Pianko-Oprych et al., 2009; Liu & Barigou, 2013).

Results show that the second order model is more prone to velocity errors than the first order model. This is due to the higher order calculations (Eqs. 7-9) involved which tend to amplify any errors in the initial experimental data used to drive the model. Both models, however, are capable of predicting the velocity information with reasonable accuracy in all three directions, with [1]LSM being moderately better. Henceforth, the velocity profiles will be discussed in terms of total velocity.

4.2.2. Occupancy

Occupancy is defined as the fraction of the total experimental time (t_∞) a tracer particle spends in each grid cell during the experiment. This definition is subject to bias due to the density of the grid and probability of tracer presence in the cells. Instead an ergodic time (t_E) is defined which is the time a tracer would spend in a cell assuming the flow is ergodic, thus (Guida et al., 2010a, 2010b, 2011; Liu & Barigou, 2013, 2015):

$$t_E = t_\infty / N_c \tag{13}$$

where, N_c is the total number of grid cells. Thus, the local occupancy can be defined as:

$$O_E = \frac{\Delta t}{t_E} \tag{14}$$

where, Δt is the time the tracer spends inside a given cell. Azimuthally-averaged plots of radially-averaged and axially-averaged occupancy are presented in Fig. 10. The experimental measurements show that the local occupancy distribution is quasi-uniform, and this is well predicted by both LSM models.

4.3. Effects of impeller configuration

In addition to the PBTD, discussed above, which is a mixed-flow 6-blade 45^o pitched-blade turbine (PBT) pumping down, we also tested the LSM models using the PBT in up-pumping mode (PBTU) as well as a radial-flow 6-blade Rushton disc turbine (RDT) for a rotational speed of 300 rpm. Between them, the flows generated by these impeller configurations represent most of the standard agitation conditions encountered in mixing vessels. Total velocity results for the PBTU, presented in Fig. 11, show that ^{2}LSM exhibits some significant underpredictions in the bottom half of the vessel below the impeller plane, especially near the bottom and the wall. ^{1}LSM exhibits only minor underpredictions in this region and overall performs moderately better than ^{2}LSM throughout the vessel.

Results for the RDT impeller are depicted in Fig. 12. Similar observations can be made as for the PBTD and PBTU above. Due to the radial flow nature of the RDT, the largest prediction errors occur just below and just above the impeller plane but, overall, both models perform well in the rest of the vessel. In conclusion, ^{1}LSM and ^{2}LSM are capable of predicting single-phase flow in a stirred vessel regardless of impeller configuration with generally good accuracy, with ^{1}LSM slightly surpassing ^{2}LSM. Therefore, in the rest of this study, we will focus solely on ^{1}LSM.

4.4. Prediction of flow conditions outside range of experimental measurements

The data used to drive the LSM can be manipulated to predict flow conditions well outside the range of experimental measurements. For instance, velocity information from a 5 min experimental trajectory obtained at 100 rpm with PBTD was multiplied by the ratio $v_{tip,500\ rpm}$ / $v_{tip,\ 100\ rpm}$, and then fed to the ^{1}LSM to predict the long-term trajectory corresponding to 500 rpm for the same PBTD. Results presented in Fig. 13 demonstrate a generally good agreement between predictions and experiment, the only significant errors (underestimations) being mainly confined to the bottom half of the vessel below the impeller plane. These errors may be attributed to the decorrelation times used in the LSM which were obtained from the 100 rpm experiment, resulting in a stochastic scaling which may not accurately represent the flow in the 500 rpm experiment, particularly in the high turbulence regions near the impeller. Nevertheless, the fact that the LSM can predict flow conditions far beyond the range of experimental measurements with such a level of accuracy is a significant achievement.

5. Conclusion

The application of a data-driven Lagrangian stochastic model based on random walk particle tracking to single-phase flow in a mechanically agitated vessel has been studied for the first time. Both first and second order models provide good predictions of local flow velocity and tracer particle occupancy, with the first order model being slightly superior. The performance of the model was studied under a range of flow conditions including different impeller configurations and rotational speeds. The model is also capable of predicting flow well outside the range of experimental conditions, for example, using initial driver data from a lower impeller speed to predict flow at a much higher speed. The technique relies on the initial input of a small set of experimental data to drive the model. Generally, a driver trajectory on the order of 1 min length is sufficient to enable adequate prediction of long-term flow trajectories. In addition to its accuracy, the LSM approach proposed here has the added advantage of being computationally efficient compared to existing modelling techniques.

Nomenclature

Symbols

a	particle acceleration (m s^{-2})
B	baffle width (m)
C_f	collision factor
C_{imp}	impeller clearance (m)
D	impeller diameter (m)
dt	time step (s)
dw	Wiener process ($s^{1/2}$)
H	height of suspension (m)
N_c	total number of cells
N_r	number of cells in radial direction
N_z	number of cells in axial direction
N_θ	number of cells in azimuthal direction
O_E	local occupancy
ϕ	particle- vessel wall collision angle
Δt	time spent by tracer particle in a cell (s)
T	tank diameter (m)
T_u, T_a	velocity and acceleration decorrelation time (s)
t_E	ergodic time (s)

t_∞	total experimental time (s)
u	particle velocity (m s^{-1})
$\overline{U}$	mean particle velocity (m s^{-1})
v	total velocity (m s^{-1})
v_1,v_2	total particle velocity prior to/after collision with vessel wall (m s^{-1})
$\mathbf{v_i}$, $\mathbf{v_r}$	particle incident/rebound velocity vector (m s^{-1})
v_{cell}	local time-averaged velocity
v_{tip}	impeller tip velocity (m s^{-1})
W	impeller width (m)
x	particle position (m)

Abbreviations

CM	collision model
LSM	Lagrangian stochastic model/modelling
PBT	pitched blade turbine
PBTD	pitched blade turbine, down-pumping
PBTU	pitched blade turbine, up-pumping
PEPT	positron emission particle tracking
RDT	Rushton disc turbine
RPI	random particle injection
RWPT	random walk particle tracking

Acknowledgement

This work was supported by EPSRC Programme Grant EP/R045046/1: Probing Multiscale Complex Multiphase Flows with Positrons for Engineering and Biomedical Applications (PI: Prof. M. Barigou, University of Birmingham).

References

Barigou, M. (2004), 'Particle Tracking in Opaque Mixing Systems: An Overview of the Capabilities of PET and PEPT', Chemical Engineering Research and Design 82(9), 1258-1267.

Bergin, M. S. & Milford, J. B. (2000), 'Application of Bayesian Monte Carlo analysis to a Lagrangian photochemical air quality model', Atmospheric Environment 34(5), 781-792.

Dehling, H. G., Dechsiri, C., Gottschalk, T., Wright, P. C. & Hoffmann, A. C. (2007), 'A stochastic model for mixing and segregation in slugging fluidized beds', Powder Technology 171(2), 118-125.

Farzaneh, M., Sasic, S., Almstedt, A.-E., Johnsson, F. & Pallarès, D. (2011), 'A novel multigrid technique for Lagrangian modeling of fuel mixing in fluidized beds', Chemical Engineering Science 66(22), 5628-5637.

Ferrero, E. & Oettl, D. (2019), 'An evaluation of a Lagrangian stochastic model for the assessment of odours', Atmospheric Environment 206, 237-246.

Gardiner, C. W. (2004), Handbook of Stochastic Methods for Physics, Chemistry, and the Natural Sciences, number 13 in 'Springer Series in Synergetics', 4th edition edn, Springer-Verlag, Berlin.

Gleicher, S. C., Chamecki, M., Isard, S. A., Pan, Y. & Katul, G. G. (2014), 'Interpreting three-dimensional spore concentration measurements and escape fraction in a crop canopy using a coupled Eulerian-Lagrangian stochastic model', Agricultural and Forest Meteorology 194, 118-131.

Guida, A., Nienow, A. W. & Barigou, M. (2010a), 'PEPT measurements of solid-liquid flow field and spatial phase distribution in concentrated monodisperse stirred suspensions', Chemical Engineering Science 65(6), 1905-1914.

Guida, A., Nienow, A. W. & Barigou, M. (2010b), 'Shannon entropy for local and global description of mixing by Lagrangian particle tracking', 65(10), 2865-2883.

Guida, A., Nienow, A. W. & Barigou, M. (2011), 'Mixing of dense binary suspensions: Multi-component hydrodynamics and spatial phase distribution by PEPT', American Institute of Chemical Engineers Journal 57(9), 2302-2315.

Israelsson, P. H., Kim, Y. D. & Adams, E. E. (2006), 'A comparison of three Lagrangian approaches for extending near field mixing calculations', Environmental Modelling & Software 21(12), 1631-1649.

Joshi, J. B. & Nayak, A. K. (2019), Advantages of Computational Fluid Dynamics in Nuclear Reactor Design and Safety Assessment, Elsevier.

LaCasce, J. H. (2008), 'Statistics from Lagrangian observations', Progress in Oceanography 77, 1-29.

Liu, L. & Barigou, M. (2013) 'Numerical modelling of velocity field and phase distribution in dense monodisperse solid–liquid suspensions under different regimes of agitation: CFD and PEPT experiments', Chemical Engineering Science, 101, pp. 837–850. doi: 10.1016/j.ces.2013.05.066.

Liu, L. & Barigou, M. (2015) 'Lagrangian particle tracking in mechanically agitated polydisperse suspensions: Multi-component hydrodynamics and spatial distribution', International Journal of Multiphase Flow, 73, pp. 80–89. doi: 10.1016/j.ijmultiphaseflow.2015.03.008.

Marshall, J. S. & Sala, K. (2011), 'A stochastic Lagrangian approach for simulating the effect of turbulent mixing on algae growth rate in a photobioreactor', Chemical Engineering Science 66(3), 384-392.

Matos, J., Brito, M. S. C. A., Dias, M. M., Lopes, J. C. B. & Santos, R. J. (2018), 'Lagrangian mixing simulation and quantification of scales', Chemical Engineering Science 192, 199-210.

Nordam, T., Kristiansen, R., Nepstad, R. & R¨ohrs, J. (2019), 'Numerical analysis of boundary conditions in a Lagrangian particle model for vertical mixing, transport and surfacing of buoyant particles in the water column', Ocean Modelling 136, 107-119.

Pianko-Oprych, P., Nienow, A. W. and Barigou, M. (2009) 'Positron emission particle tracking (PEPT) compared to particle image velocimetry (PIV) for studying the flow generated by a pitched-blade turbine in single phase and multi-phase systems', Chemical Engineering Science, 64(23), pp. 4955–4968. doi: 10.1016/j.ces.2009.08.003.

Rezavand, M., Winkler, D., Sappl, J., Seiler, L., Meister, M. & Rauch, W. (2019), 'A fully Lagrangian computational model for the integration of mixing and biochemical reactions in anaerobic digestion', Computers & Fluids 181, 224-235.

Ruplo, V. (2006), 'A Lagrangian-Based Approach for Determining Trajectories Taxonomy and Turbulence Regimes', Journal of Physical Oceanography 37, 1584-1609.

Sadrmomtaz, A., Parker, D. & Byars, L. (2007), 'Modification of a medical PET scanner for PEPT studies', Nuclear Instruments and Methods in Physics Research 573(1-2), 91-94.

Thomson, D. J. (1987), 'Criteria for the selection of stochastic models of particle trajectories in turbulent flows', Journal of Fluid Mechanics 180, 529-556.

Figure and Table captions

Fig. 1. Schematic of experimental setup: (a) mixing vessel and PEPT γ-ray detectors; (b) computational grid consisting of N_r cells in the r-direction, N_z cells in the z-direction and N_θ cells in the θ–direction; (c) method of calculation of local time-averaged velocity v_{cell} in the i^{th} cell.

Fig. 2. Flowchart of LSM algorithm: showing collision model (CM) and random particle injection (RPI) methods of re-inserting model particles into the domain.

Fig. 3. Effect of grid mesh density on number of detected positions in each cell: Sample results shown are based on 5 min-long experimental PEPT trajectories for one layer of cells in the θ-direction (N_θ = 12); white cells have no detected positions; agitation speed = 300 rpm, PBTD configuration.

Fig. 4. Histograms of PEPT particle tracer-wall collision factor, C_f, for experiments using PBTD configuration at 100 and 500 rpm: (a) $C_f = \frac{v_2}{v_1}$; (b) $C_f = \frac{1}{\tan(\phi)}$.

Fig. 5. Sensitivity analysis of LSM-predicted time-averaged velocity profiles in cells adjacent to the vessel wall to the value of C_f adopted: experimental and modelling data shown are for 40 min trajectory obtained at 300 rpm with PBTD configuration: (a) $C_f = \frac{v_2}{v_1}$; (b) $C_f = \frac{1}{\tan(\phi)}$.

Fig. 6. Effects of length of LSM driver trajectory on azimuthally averaged profiles of total velocity predicted: PEPT and [1]LSM compared at 300 rpm with PBTD configuration.

Fig. 7. Azimuthally averaged profiles of local θ-velocity component: PEPT, [1]LSM and [2]LSM compared at 300 rpm with PBTD configuration.

Fig. 8. Azimuthally averaged profiles of local *z*-velocity component: PEPT, [1]LSM and [2]LSM compared at 300 rpm with PBTD configuration.

Fig. 9. Azimuthally averaged profiles of local *r*-velocity component: PEPT, [1]LSM and [2]LSM compared at 300 rpm with PBTD configuration.

Fig. 10. Azimuthally averaged plots of (a) radially-averaged and (b) axially-averaged occupancy: PEPT, [1]LSM and [2]LSM compared at 300 rpm with PBTD configuration.

Fig. 11. Azimuthally averaged profiles of total velocity: PEPT, [1]LSM and [2]LSM compared at 300 rpm with PBTU configuration.

Fig. 12. Azimuthally averaged profiles of total velocity: PEPT, [1]LSM and [2]LSM compared at 300 rpm with RDT configuration.

Fig. 13. Azimuthally averaged profiles of total velocity for 500 rpm PBTD predicted on the basis of 5 min initial data from 100 rpm PBTD experiment: PEPT and [1]LSM.

Table 1. Velocity and acceleration decorrelation times for minute intervals of experimental at 500 rpm PBTD PEPT data.

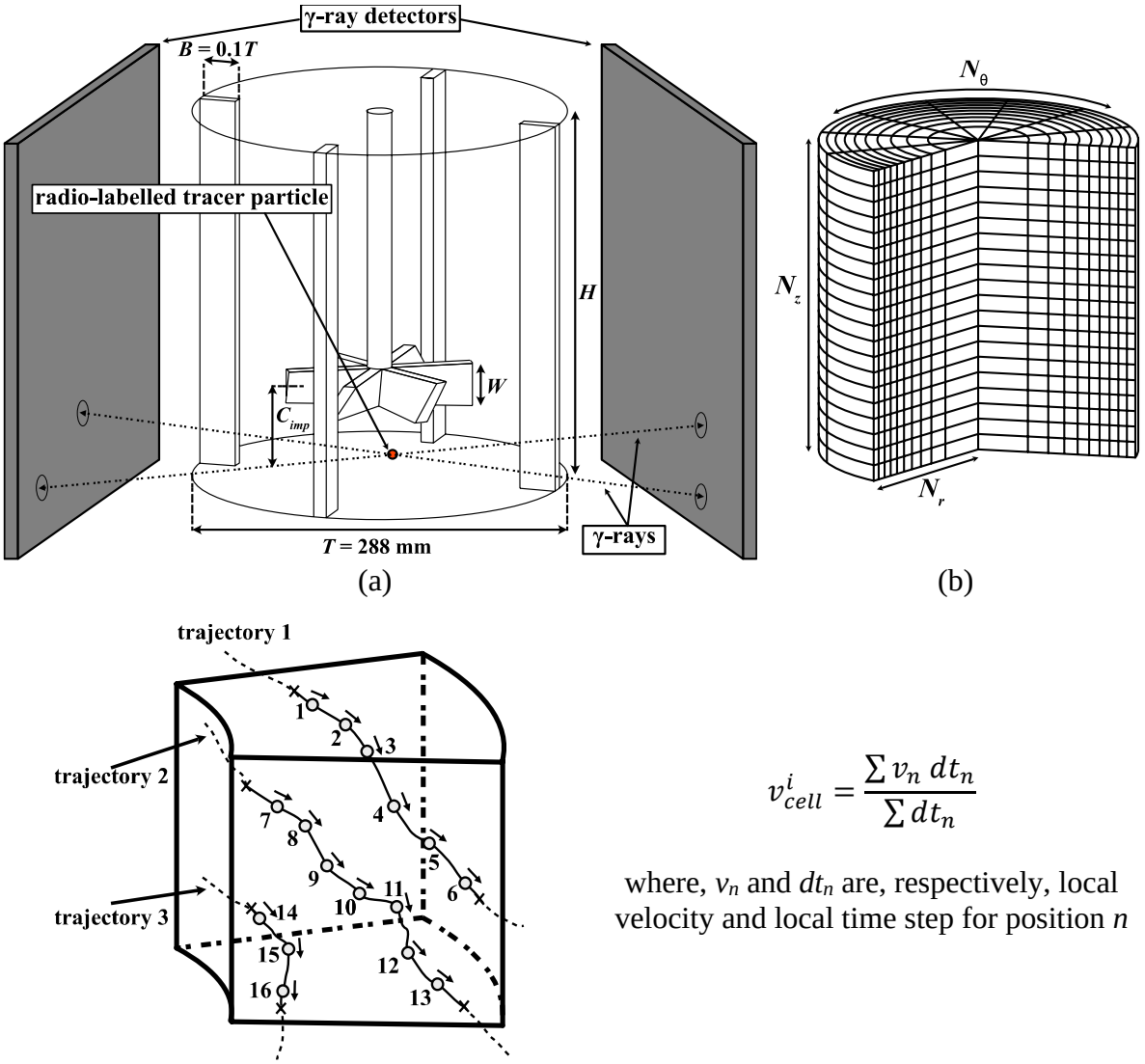

$$v_{cell}^{i} = \frac{\sum v_n \, dt_n}{\sum dt_n}$$

where, v_n and dt_n are, respectively, local velocity and local time step for position n

Fig. 1. Schematic of experimental setup: (a) mixing vessel and PEPT γ-ray detectors; (b) computational grid consisting of N_r cells in the r-direction, N_z cells in the z-direction and N_θ cells in the θ–direction; (c) method of calculation of local time-averaged velocity v_{cell} in the i^{th} cell.

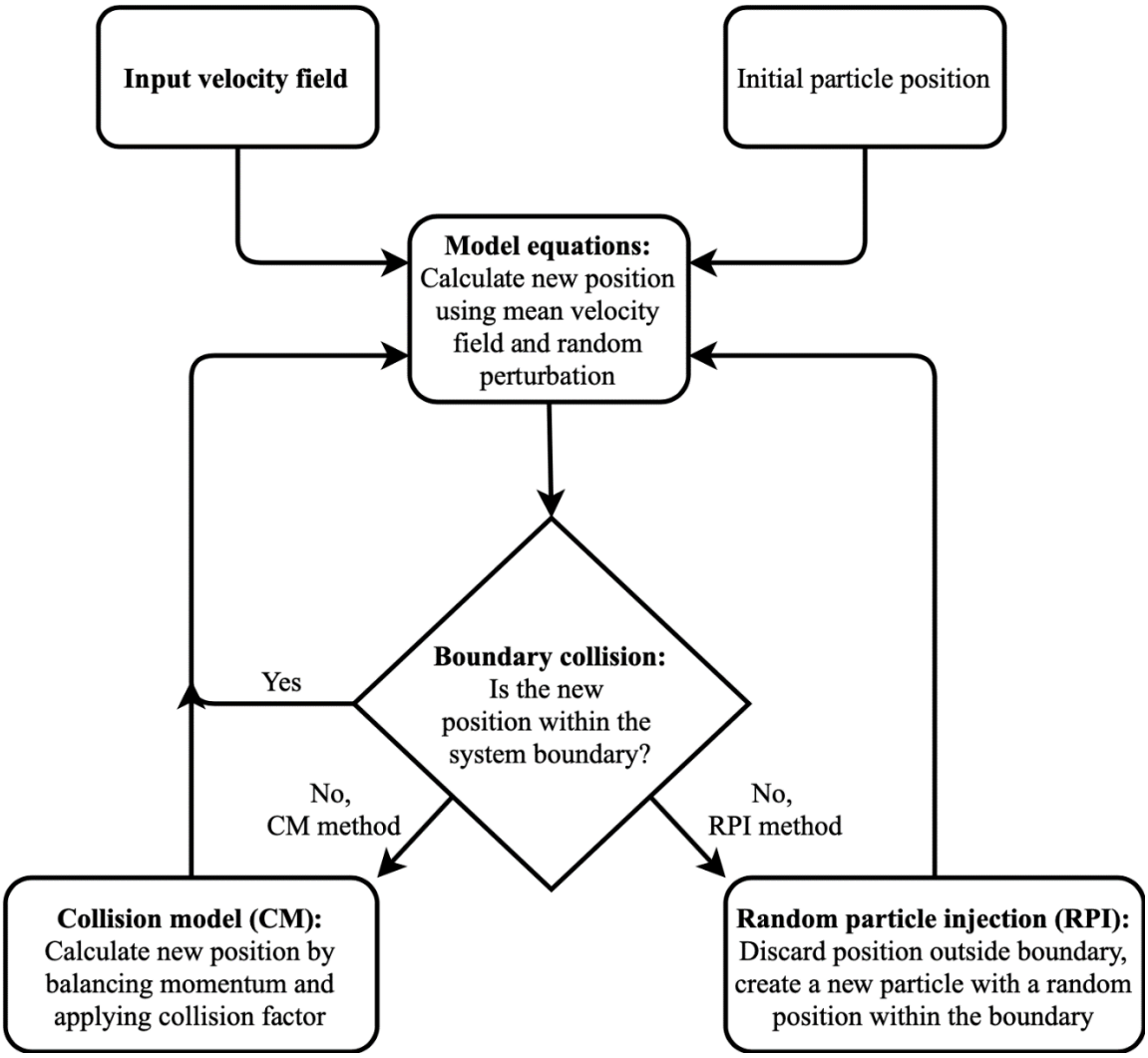

Fig. 2. Flowchart of LSM algorithm: showing collision model (CM) and random particle injection (RPI) methods of re-inserting model particles into the domain.

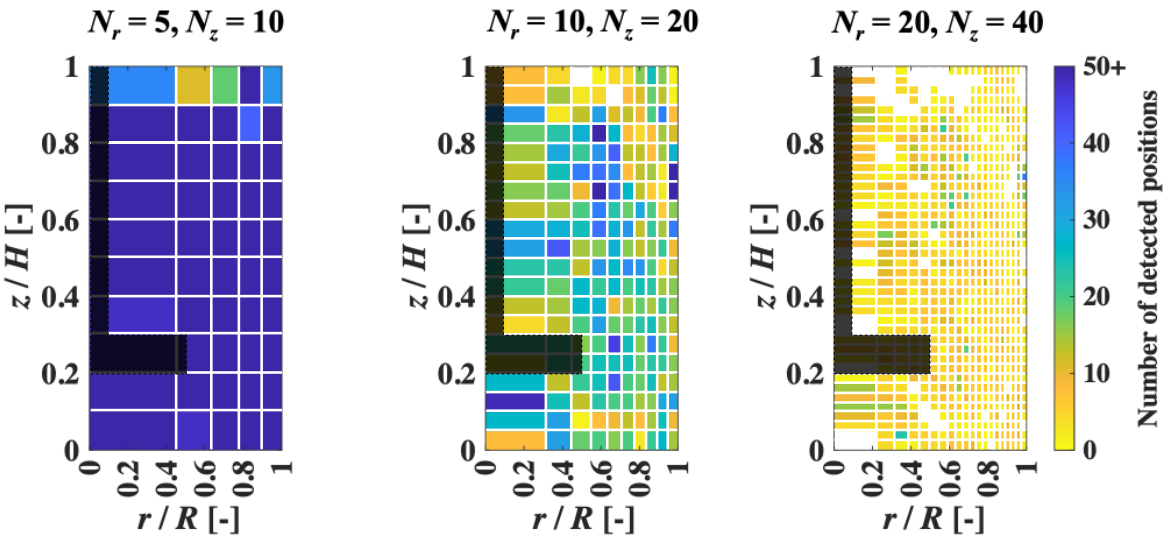

Fig. 3. Effect of grid mesh density on number of detected positions in each cell: Sample results shown are based on 5 min-long experimental PEPT trajectories for one layer of cells in the θ-direction (N_θ = 12); white cells have no detected positions; agitation speed = 300 rpm, PBTD configuration.

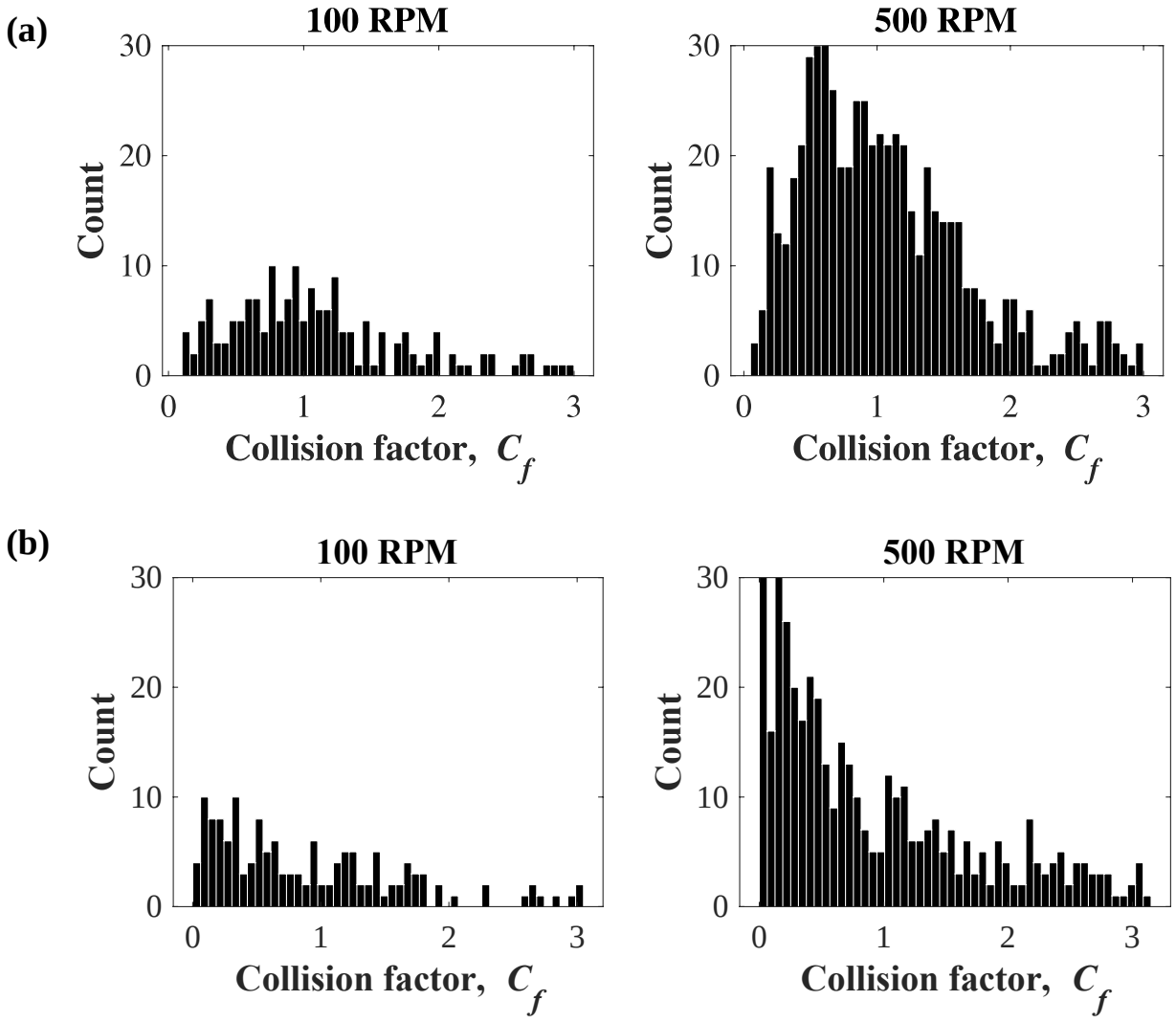

Fig. 4. Histograms of PEPT particle tracer-wall collision factor, C_f, for experiments using PBTD configuration at 100 and 500 rpm: (a) $C_f = \frac{v_2}{v_1}$; (b) $C_f = \frac{1}{\tan(\phi)}$.

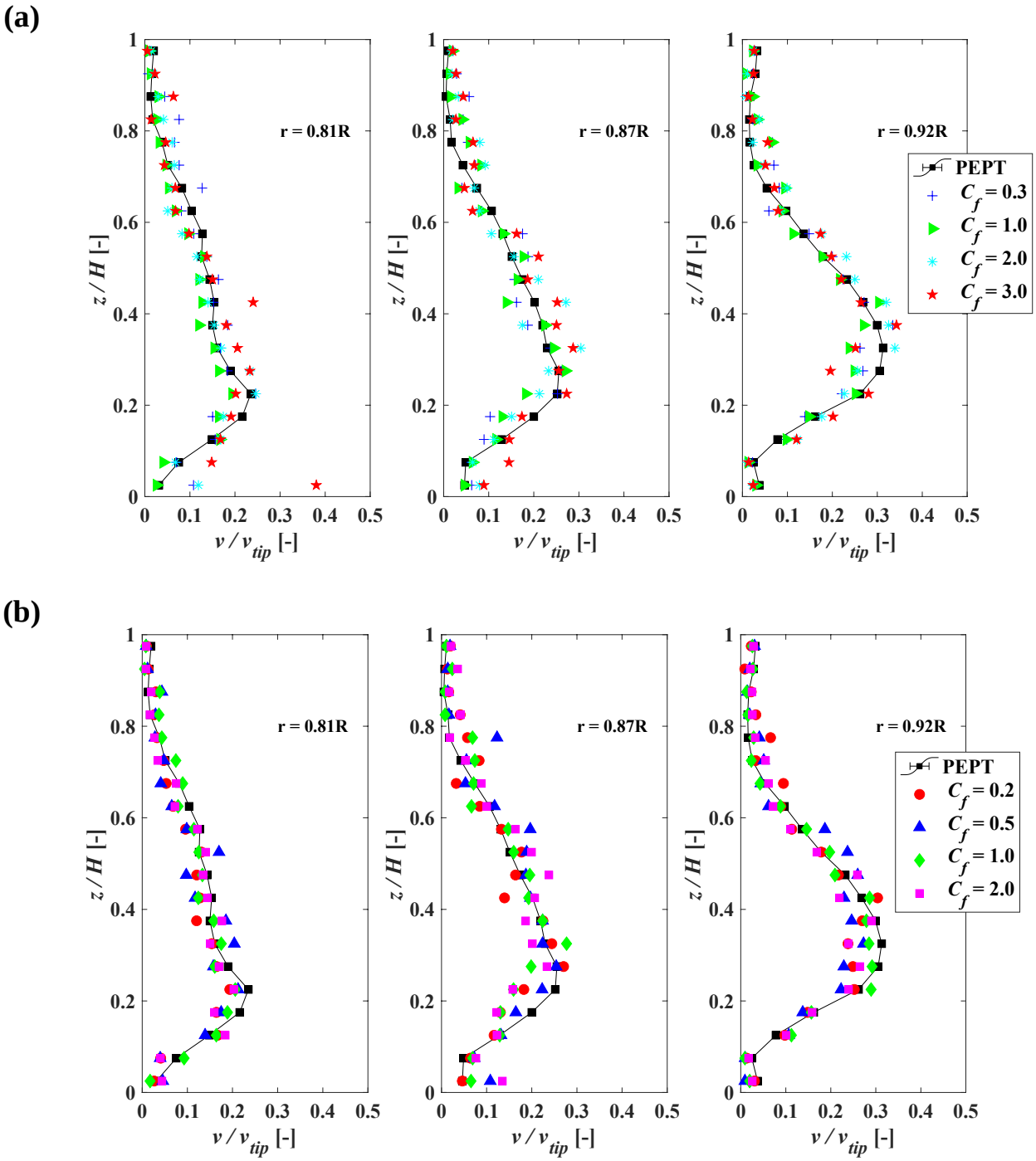

Fig. 5. Sensitivity analysis of LSM-predicted time-averaged velocity profiles in cells adjacent to the vessel wall to the value of C_f adopted: experimental and modelling data shown are for 40 min trajectory obtained at 300 rpm with PBTD configuration: (a) $C_f = \frac{v_2}{v_1}$; (b) $C_f = \frac{1}{\tan(\phi)}$.

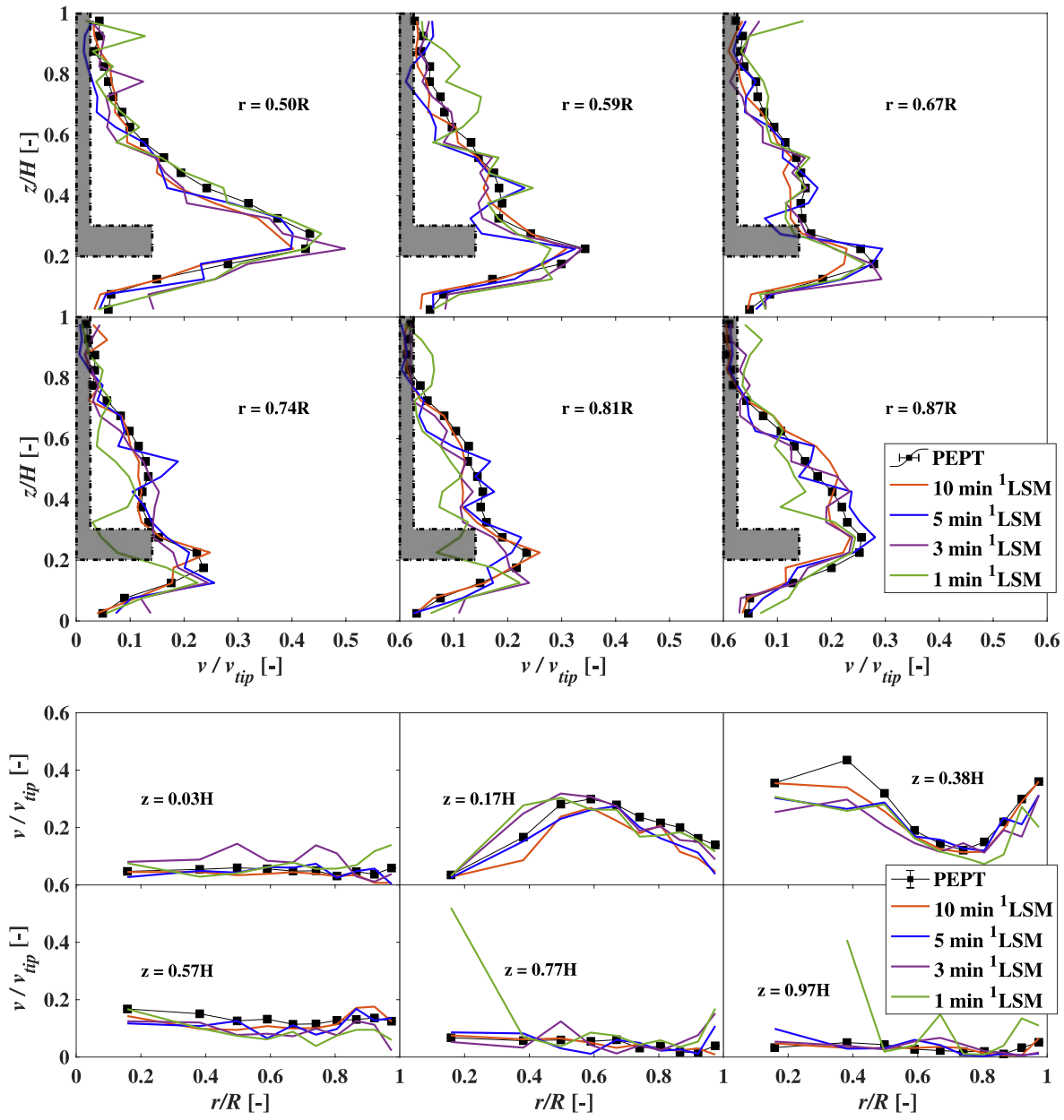

Fig. 6. Effects of length of LSM driver trajectory on azimuthally averaged profiles of total velocity predicted: PEPT and ^{1}LSM compared at 300 rpm with PBTD configuration.

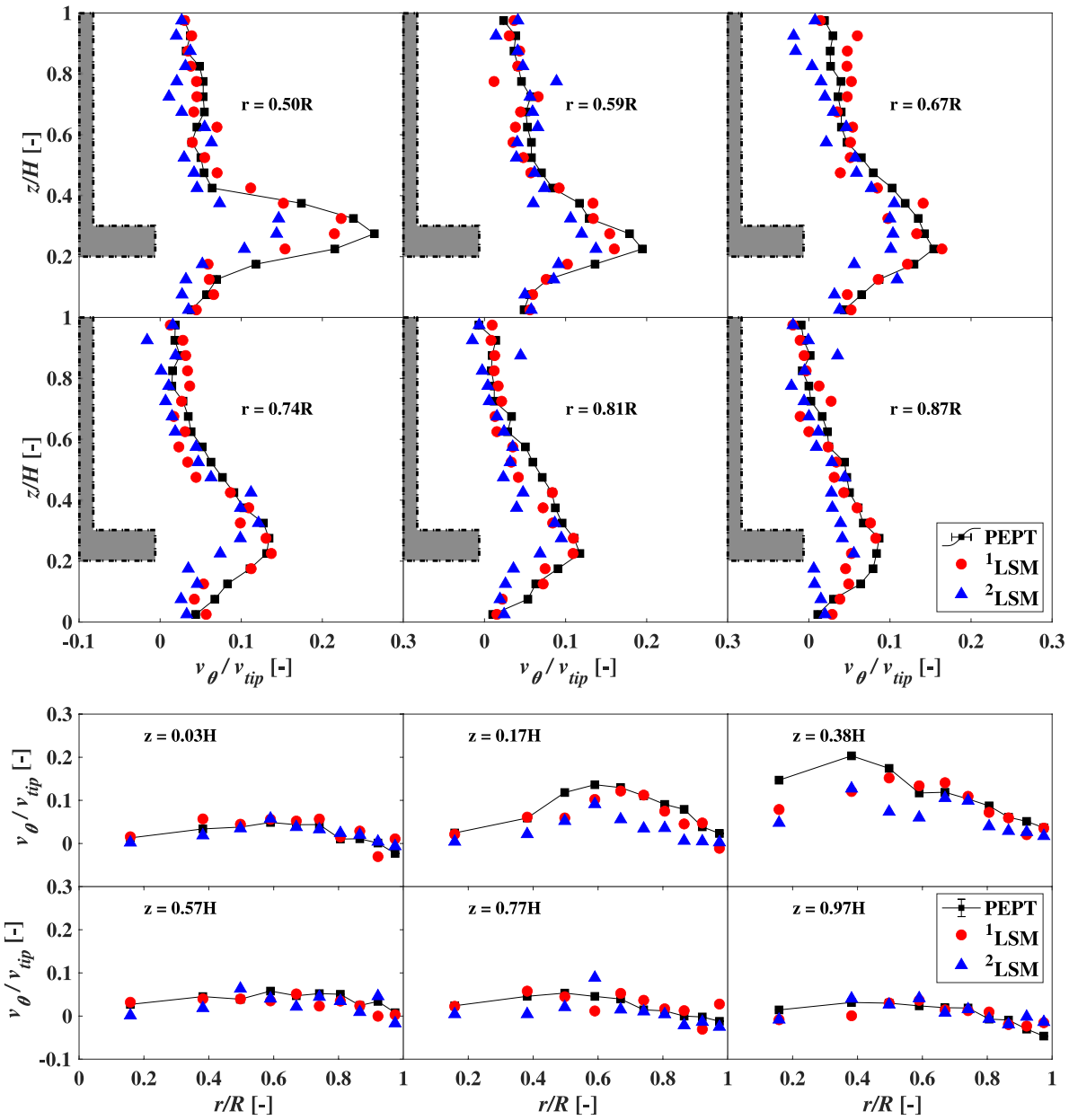

Fig. 7. Azimuthally averaged profiles of local θ-velocity component: PEPT, [1]LSM and [2]LSM compared at 300 rpm with PBTD configuration.

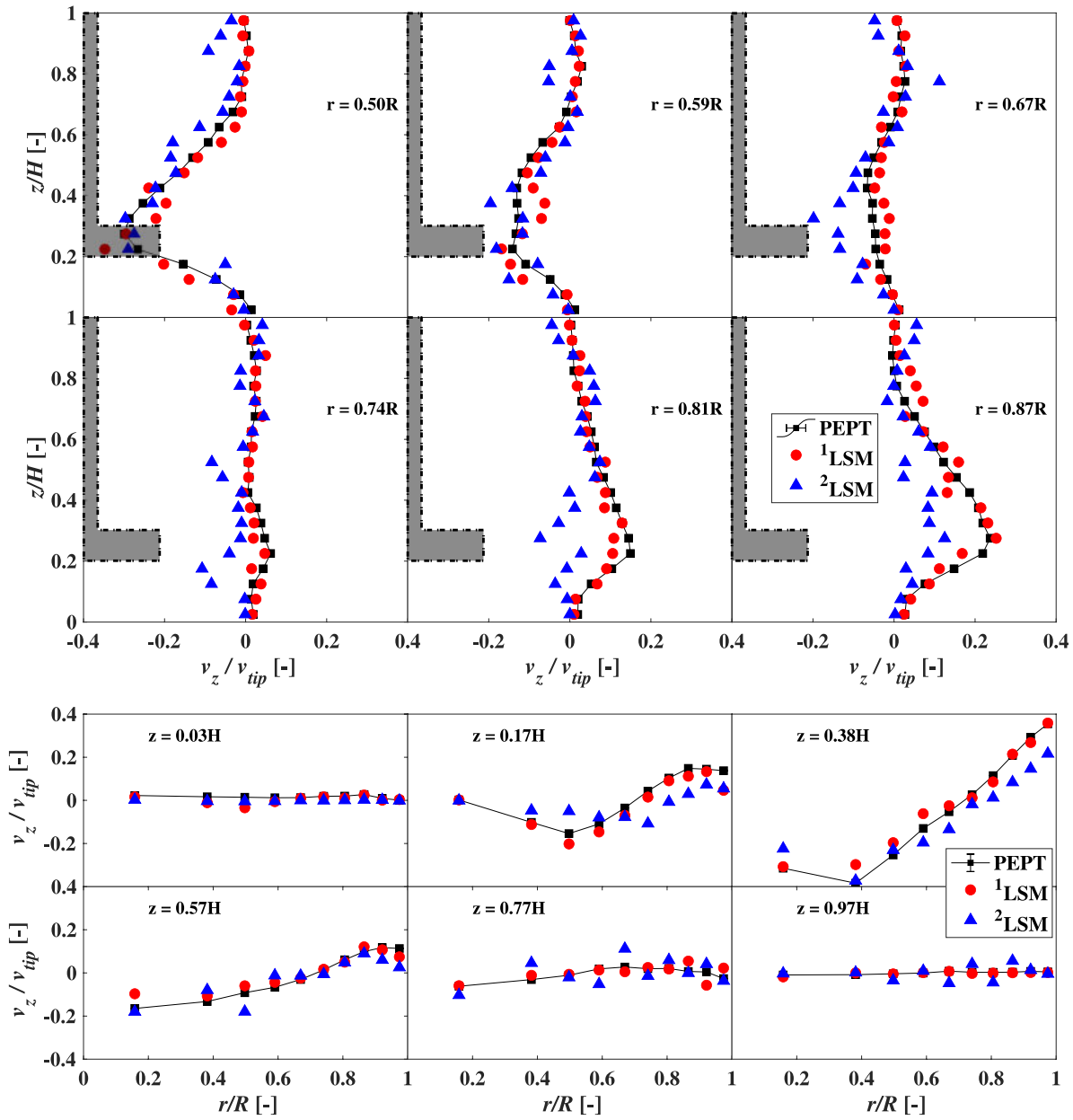

Fig. 8. Azimuthally averaged profiles of local *z*-velocity component: PEPT, [1]LSM and [2]LSM compared at 300 rpm with PBTD configuration.

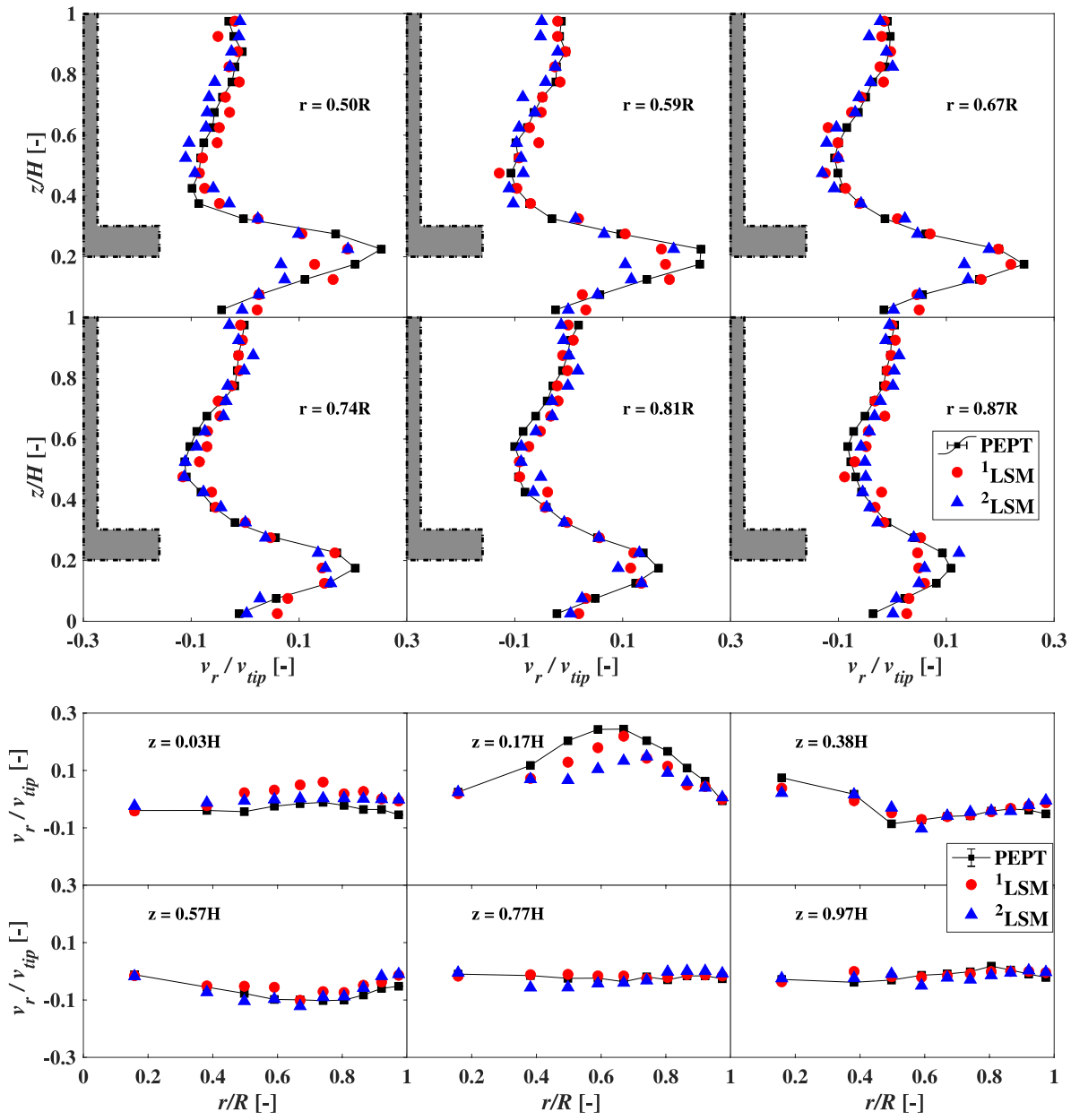

Fig. 9. Azimuthally averaged profiles of local *r*-velocity component: PEPT, [1]LSM and [2]LSM compared at 300 rpm with PBTD configuration.

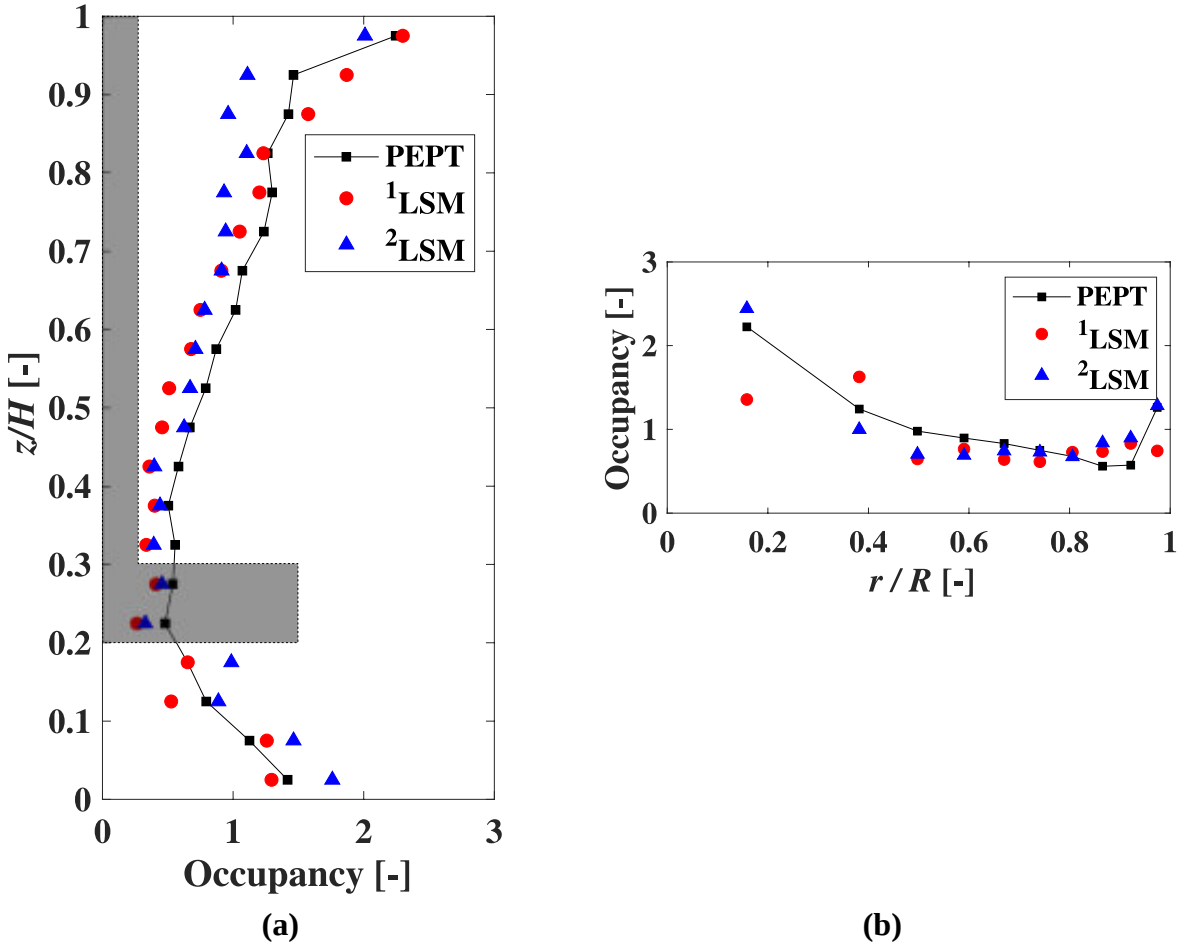

Fig. 10. Azimuthally averaged plots of (a) radially-averaged and (b) axially-averaged occupancy: PEPT, [1]LSM and [2]LSM compared at 300 rpm with PBTD configuration.

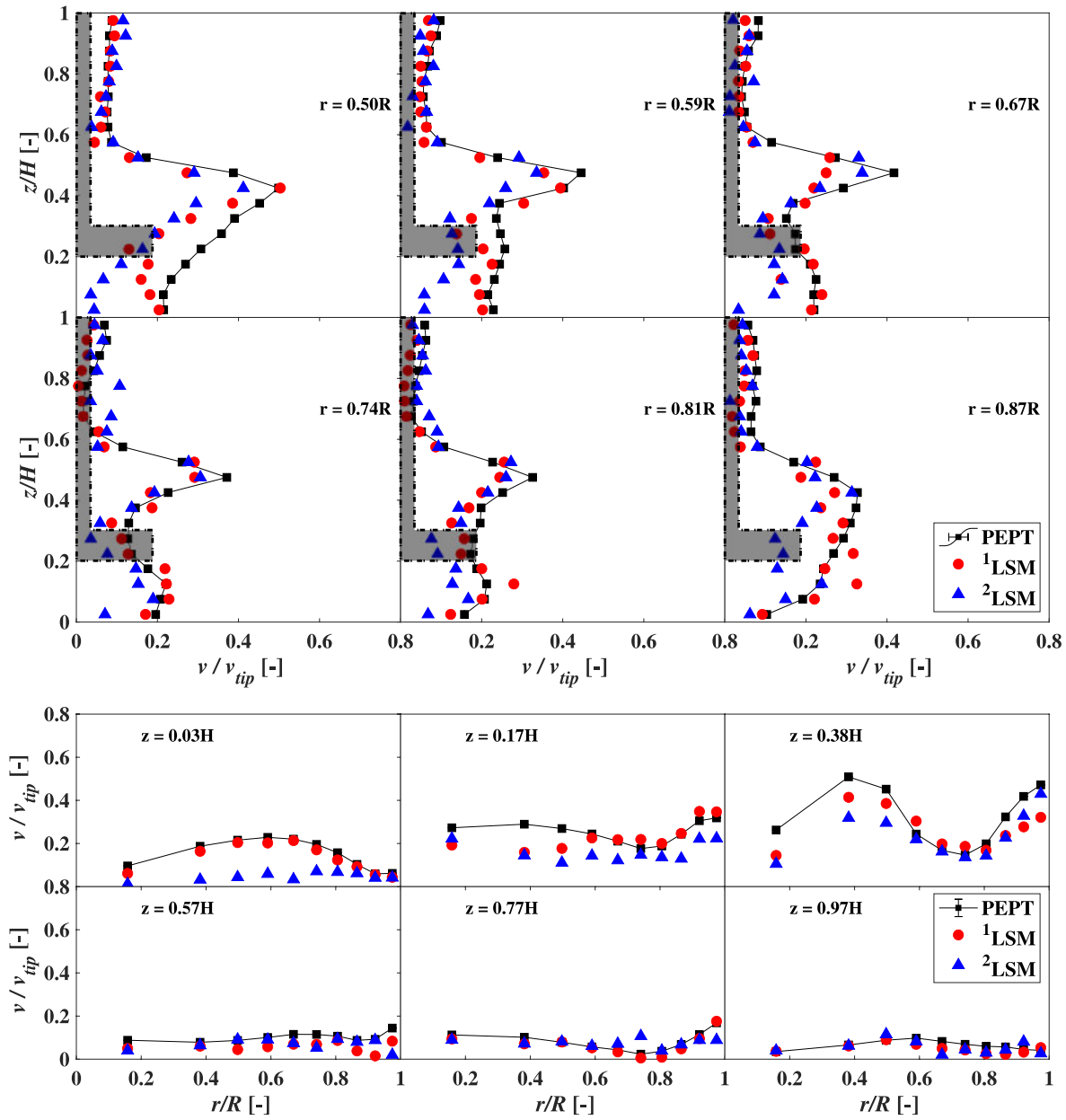

Fig. 11. Azimuthally averaged profiles of total velocity: PEPT, [1]LSM and [2]LSM compared at 300 rpm with PBTU configuration.

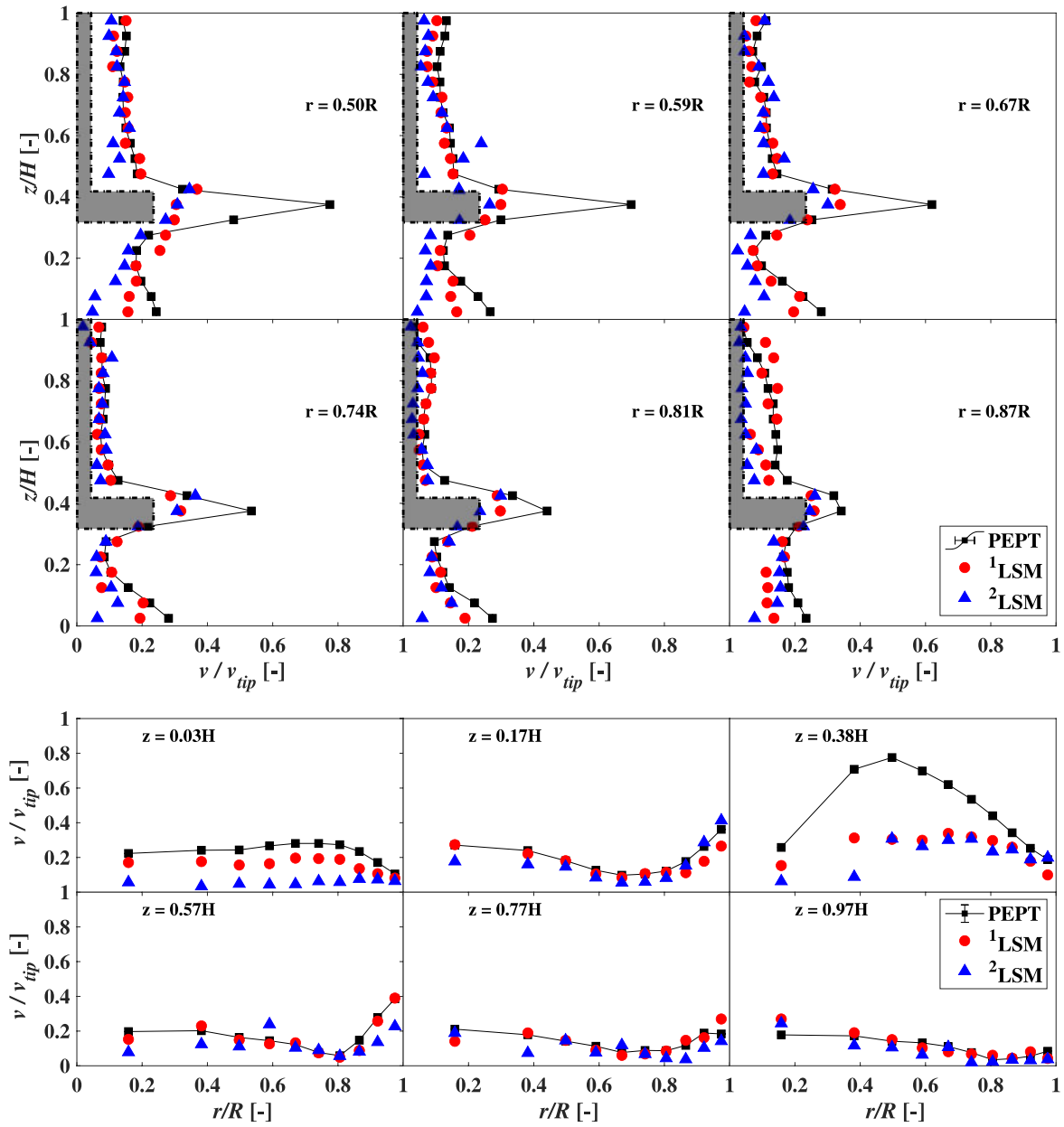

Fig. 12. Azimuthally averaged profiles of total velocity: PEPT, [1]LSM and [2]LSM compared at 300 rpm with RDT configuration.

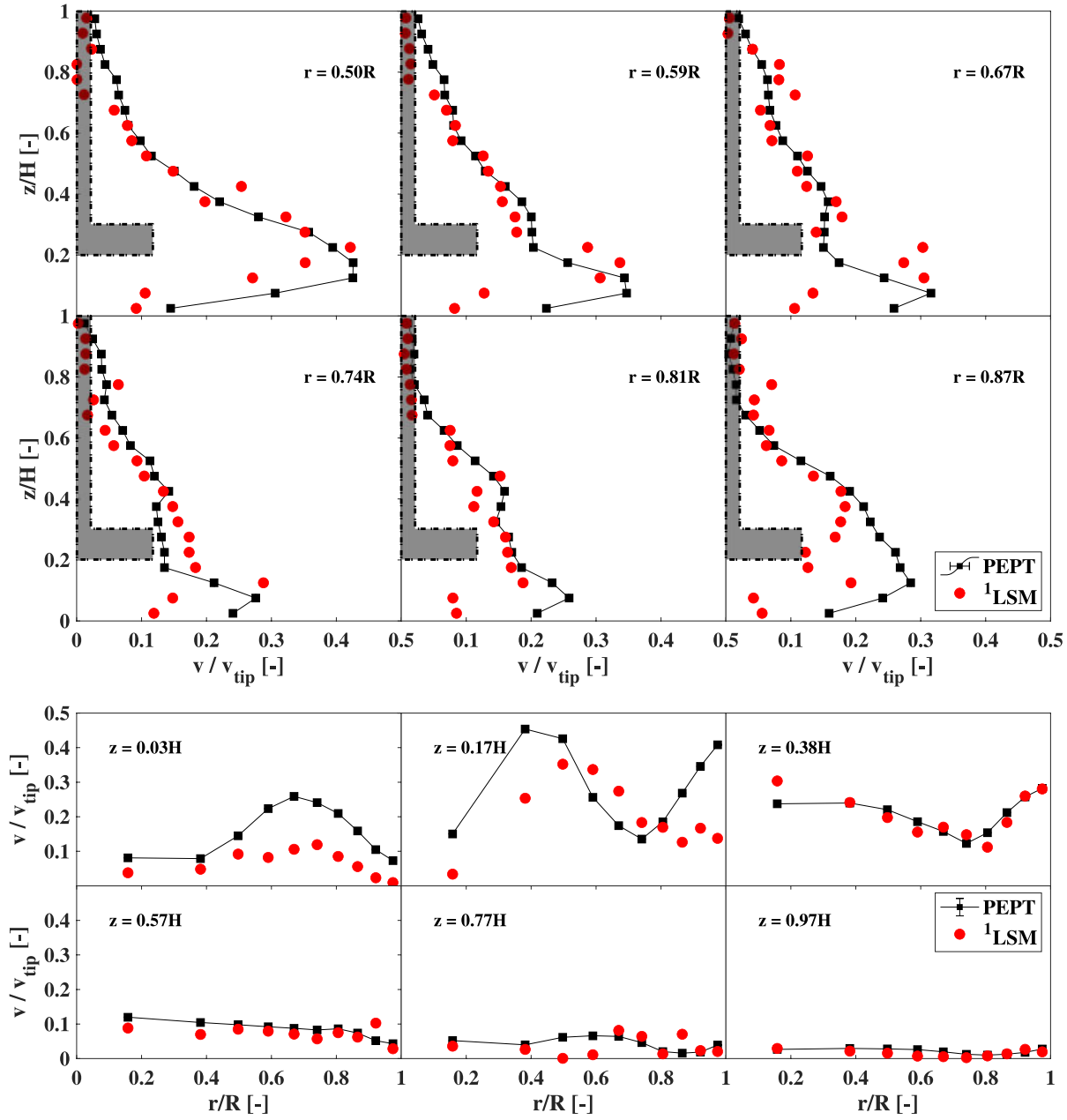

Fig. 13. Azimuthally averaged profiles of total velocity for 500 rpm PBTD predicted on the basis of 5 min initial data from 100 rpm PBTD experiment: PEPT and [1]LSM.

Table 1. Velocity and acceleration decorrelation times for minute intervals of experimental at 500 rpm PBTD PEPT data.

	Decorrelation time (ms)					
T (min)	v_x	v_y	v_z	a_x	a_y	a_z
0-1	40	57	24	23	24	23
1-2	38	60	25	23	23	23
2-3	42	69	25	24	24	23
3-4	41	63	25	25	24	23
4-5	42	64	25	24	24	23
average value	**41**	**63**	**25**	**24**	**24**	**23**